JOURNAL OF AIRCRAFT
Vol. 47, No. 2, March–April 2010

Nonlinear-Aerodynamics/Nonlinear-Structure Interaction Methodology for a High-Altitude Long-Endurance Wing

Z. Wang,* P. C. Chen,† and D. D. Liu‡
Zona Technology, Inc., Scottsdale, Arizona 85258
and
D. T. Mook§
Virginia Polytechnic Institute and State University, Blacksburg, Virginia 24061

DOI: 10.2514/1.45694

Nonlinear aeroelastic analysis is essential for high-altitude long-endurance (HALE) aircraft. In the current paper, we have presented a computational aeroelastic tool for nonlinear-aerodynamics/nonlinear-structure interaction. Specifically, a consistent nonlinear time-domain aeroelastic methodology has been integrated via tightly coupling a geometrically exact nonlinear intrinsic beam model and the generalized unsteady vortex-lattice aerodynamic model with vortex roll-up and free wake. The effects of discrete gust as well as flow separation at various angles of attack from attached flow to the stall and poststall ranges are also included in the nonlinear aerodynamic model. A HALE-wing model is analyzed as a numerical example. The trim angle of attack is first found for the wing, and the results show that aeroelastic instability could occur at higher angles of attack. The HALE-wing model under the trim condition is then analyzed for various gust profiles to which it is subject. It is found that for certain gust levels, the elastic deformations of the HALE wing tend to become unstable: notably, the in-plane deflections become very significant. It is noted for the unstable solution of the HALE wing that the flow may be well beyond the stall range. An engineering approach with the use of the nonlinear sectional lift is attempted to consider such stall effects.

Nomenclature

C	=	coordinate transformation matrix between undeformed and deformed beam cross-sectional systems
F	=	cross-sectional stress resultant force vector
f	=	distributed applied force vector per unit length along the beam
G	=	circulation associated with each vortex panel
H	=	cross-sectional inertial angular momentum vector
I	=	cross-sectional inertial matrix, dimension (3×3)
M	=	cross-sectional stress resultant moment vector
m	=	distributed applied moment vector per unit length along the beam
P	=	cross-sectional inertial linear momentum vector
R, S, T	=	cross-sectional flexibility coefficient matrices (3×3)
V	=	linear velocity vector
α_{eff}	=	effective angle of attack at each strip
Γ	=	circulation around vortex segment
γ	=	extensional and transverse shear strain measure vector
ξ	=	offset vector of the cross-sectional mass centroid from the reference line
κ	=	torsional deformation and bending curvature vector
μ	=	mass per unit length along the beam
Φ	=	flow velocity potential
Ω	=	angular velocity vector

Presented as Paper 2106 at the 48th AIAA/ASME/ASCE/AHS/ASC Structures, Structural Dynamics, and Materials Conference, Honolulu, HI, 23–26 April 2007; received 27 May 2009; revision received 5 October 2009; accepted for publication 26 October 2009.

*Research and Development Engineering Specialist, 9489 East Ironwood Square Drive. Member AIAA.

†Vice President, 9489 East Ironwood Square Drive. Member AIAA.

‡President, 9489 East Ironwood Square Drive. Fellow AIAA.

§N. Waldo Harrison Professor Emeritus, Department of Engineering Science and Mechanics. Associate Fellow AIAA.

I. Introduction

NONLINEAR aeroelastic analysis is essential for high-altitude long-endurance (HALE) aircraft. The HALE wings are likely very sizable, and hence flexible, in order to achieve the necessary aerodynamic efficiency, and so a nonlinear structural model that can account for large deflections becomes a necessity. The mishap report of Helios [1] especially points out the importance of time-domain nonlinear aeroelastic analysis for such HALE aircraft. In light of this, a nonlinear, geometrically exact, intrinsic beam model is tightly coupled with a nonlinear unsteady vortex-lattice model (UVLM) to present a totally nonlinear approach for HALE-wing aeroelastic analysis. We call it NANSI, which stands for nonlinear-aerodynamics/nonlinear-structure interaction. The governing equations of the coupled dynamic system are integrated simultaneously and interactively to yield wing-response solutions in the time domain.

In addition, the current paper describes our continuing efforts in extending NANSI to include the effects of discrete gust as well as flow separation at various angles of attack from attached flow to the stall and poststall ranges. Aeroelastic gust response analysis mostly consists of two types of analyses: the first is dynamic responses to a discrete gust and the second is dynamic responses to continuous atmospheric turbulence. The second type of gust analyses has mostly been solved by using the statistical concepts. In consistence with our time-domain aeroelastic analysis, we will focus on the discrete-gust problem only in this paper.

Discrete-gust analysis to take into account the aeroelastic effects has typically relied on frequency-domain analysis first, then used the rational function approximation method or inverse Fourier transformation to extract a time-domain solution for aeroservoelastic (ASE) analysis [2,3]. Raveh [4] has recently developed a reduced-order modeling for gust response based on computational fluid dynamics (CFD) solutions. Time-domain ROMs of the autoregessive-moving-average type were identified from a set of CFD input–output data. In this paper, the gust implementation is straightforward in the time-domain aerodynamic model employed here: namely, the general UVLM. The effects of gust on the trailing wake are well captured, as we will show later.

On the other hand, flow separation on wings/airfoils at and beyond stall has been a challenging endeavor in aerodynamics and aeroelasticity. A proper modeling of this type of flow, steady or unsteady, has been lacking in the past. Extending Prandtl's lifting-line theory (LLT) to include flow separation has been the common approach: notably, the work of Schairer [5], Levinsky [6], and van Dam et al. [7]. These approaches, different from Tani's [8] original method, lies in their choice of various versions of LLT as a basic aerodynamic model, e.g., the extended LLT, or simplified LLT. Recent work of Mukherjee et al. [9] proposed a so-called decambering approach, in which the cross-sectional profile is defined by two decambering angles. The incompressible flow solver is repeated so that a set of suitable decambering angles is obtained for each section. With such an updated wing geometry, the sectional lift predicted by the lifting-surface method matches with those found with the known sectional-lift curve. The iterative nature of the above-mentioned approaches can be cumbersome for nonlinear aeroelastic analysis, which usually already involves an iterative procedure during the time-marching process. At the same time, the use of a known sectional-lift curve is, at most, a lower-order approximation to a complicated problem such as stall. In this paper, an engineering approach is investigated by coupling the three-dimensional UVLM with the known two-dimensional sectional flow solutions for predicting the aerodynamic characteristics of a HALE wing near and beyond stall.

The organization of this paper is as follows: In Sec. II, the governing equations of the nonlinear intrinsic beam model and their spatial discretization based on finite element method are briefly introduced. In Secs. III and IV, the general unsteady vortex-lattice aerodynamic model and the discrete-gust implementation are described. In Sec. V, validation of gust analysis through Goland wing and numerical-simulation results for a HALE-wing model are presented. Section VI describes the stall modeling as well as numerical results. Finally, conclusions and remarks are given in Sec. VII.

II. Nonlinear Intrinsic Beam Model

To keep this paper as self-contained as possible, the structural model is briefly summarized here. As opposed to the classical beam theory, the equations of motion [10] developed in the intrinsic beam model are written in a compact matrix form without any approximation to the geometry of the deformed beam reference line or to the orientation of the intrinsic cross-sectional frame, and they are as follows:

$$\begin{cases} F' + (\tilde{k}+\tilde{\kappa})F + f = \dot{P} + \tilde{\Omega}P \\ M' + (\tilde{k}+\tilde{\kappa})M + (\tilde{e}_1+\tilde{\gamma})F + m = \dot{H} + \tilde{\Omega}H + \tilde{V}P \\ V' + (\tilde{k}+\tilde{\kappa})V + (\tilde{e}_1+\tilde{\gamma})\Omega = \dot{\gamma} \\ \Omega' + (\tilde{k}+\tilde{\kappa})\Omega = \dot{\kappa} \\ V = C\dot{u} \\ \Omega = R\dot{\theta} \end{cases} \tag{1}$$

Equation (1) is, in fact, expressed in each cross-sectional deforming system, denoted as the B-system. The B-system is initially aligned with the undeformed b-system, which is shown in Fig. 1. (Note that the aerodynamic coordinate system may be different from the structural coordinate system.) The cross-sectional constitutive laws are given by

$$\begin{Bmatrix} \gamma \\ \kappa \end{Bmatrix} = \begin{bmatrix} R & S \\ S^T & T \end{bmatrix} \begin{Bmatrix} F \\ M \end{Bmatrix}; \qquad \begin{Bmatrix} P \\ H \end{Bmatrix} = \begin{bmatrix} \mu\Delta & -\mu\tilde{\xi} \\ \mu\tilde{\xi} & I \end{bmatrix} \begin{Bmatrix} V \\ \Omega \end{Bmatrix} \tag{2}$$

where $F = [F_1 \quad F_2 \quad F_3]^T$ and $M = [M_1 \quad M_2 \quad M_3]^T$ are column matrices with elements as the measure numbers of cross-sectional stress and moment resultants in the basis of the deformed beam cross-sectional frame; $\gamma = [\gamma_{11} \quad 2\gamma_{12} \quad 2\gamma_{13}]^T$, where γ_{11} is the extensional measure and $2\gamma_{1\alpha}$ are the transverse shear strain measures; $\kappa = [\kappa_1 \quad \kappa_2 \quad \kappa_3]^T$, where κ_1 is the torsional deformation measure and κ_α being the bending deformation measures; $P = [P_1 \quad P_2 \quad P_3]^T$ and $H = [H_1 \quad H_2 \quad H_3]^T$ are the linear and angular momentum measures; $V = [V_1 \quad V_2 \quad V_3]^T$ and $\Omega = [\Omega_1 \quad \Omega_2 \quad \Omega_3]^T$ are the linear and angular velocity measures; f and m are distributed force and moment measures per unit length expressed in the basis of the deformed beam cross-sectional frame; $u = [u_1 \quad u_2 \quad u_3]^T$ are the displacements; $\theta = [\theta_1 \quad \theta_2 \quad \theta_3]^T$ are Rodrigues parameters; Δ is the identity matrix; and

$$C = \frac{(1-\frac{1}{4}\theta^T\theta)\Delta - \tilde{\theta} + \frac{1}{2}\theta\theta^T}{1+\frac{1}{4}\theta^T\theta} \qquad R = \frac{\Delta - (\tilde{\theta}/2)}{1+\frac{1}{4}\theta^T\theta} \tag{3}$$

The tilde is the cross-product operator.

The last two terms in Eq. (1) are needed for the sake of the aerodynamic model to solve for the aerodynamic contributions to the f and m terms in the equation; otherwise, they are not required for solving the equations. The coefficients in Eq. (2) are cross-sectional flexibility coefficients, μ is the mass per unit length, $\xi = [0 \quad \bar{x}_2 \quad \bar{x}_3]^T$ is the offset vector of the cross-sectional mass centroid from the reference line (usually the elastic axis), and I is the cross-sectional mass moment-of-inertia matrix.

By using the generalized Galerkin method and finite element basis functions, we discretize the governing equations of the nonlinear structural beam model and transform the partial differential equations into a set of ordinary differential equations (ODEs). The Galerkin method starts from the weak-form formulation. Taking one component form from Eq. (1), for example,

$$\begin{aligned} \mu\dot{V}_1 + \mu\xi_3\dot{\Omega}_2 - \mu\xi_2\dot{\Omega}_3 &= F_1' - (k_3+\kappa_3)F_2 + (k_2+\kappa_2)F_3 \\ &\quad + f_1 + \Omega_3 P_2 - \Omega_2 P_3 \end{aligned} \tag{4}$$

Set the test function ϕ: $[0, L] \to R$ to be a smooth function such that $\phi(0) = 0$. Multiplying both sides of Eq. (4) by ϕ and integrating the resulting equation over the domain $(0, L)$, we obtain

$$\begin{aligned} \int_0^L \phi[\mu\dot{V}_1 + \mu\xi_3\dot{\Omega}_2 - \mu\xi_2\dot{\Omega}_3]\,\mathrm{d}x &= -\int_0^L \phi' F_1\,\mathrm{d}x + \int_0^L \phi[-(k_3 \\ &\quad + \kappa_3)F_2 + (k_2+\kappa_2)F_3 + f_1 + \Omega_3 P_2 - \Omega_2 P_3]\,\mathrm{d}x \end{aligned} \tag{5}$$

Here, we have used integration by parts for terms involved with the spatial derivative of F_1 and have substituted for the natural boundary conditions prescribed at the end $x = L$. The weak formation of the problem defined by Eq. (1) and boundary conditions can be stated as follows: Find V, Ω, γ, and κ such that the integral equations, such as Eq. (5), hold for every ϕ.

The finite element method (FEM) comes into the picture when choosing the basis functions. We divide the beam into a finite number of elements. Linear Lagrangian basis functions are then chosen for all the primary variables, V, Ω, γ, and κ. Thus, in an element between x_j and x_{j+1}, the primary variables are assumed to be a linear function of their nodal values. With the linear Lagrangian basis functions, we can arrive at the following equations after a series of algebra manipulations:

$$\begin{bmatrix} M_{V_1} & 0 & 0 & 0 & M_{V_1}^{\Omega_2} & M_{V_1}^{\Omega_3} \\ 0 & M_{V2} & 0 & M_{V_2}^{\Omega_1} & 0 & M_{V_2}^{\Omega_3} \\ 0 & 0 & M_{V3} & 0 & M_{V_3}^{\Omega_2} & M_{V_3}^{\Omega_3} \\ 0 & M_{\Omega_1}^{V_2} & M_{\Omega_1}^{V_3} & M_{\Omega_1} & 0 & 0 \\ M_{\Omega_2}^{V_1} & 0 & M_{\Omega_2}^{V_3} & 0 & M_{\Omega_2} & 0 \\ M_{\Omega_3}^{V_1} & M_{\Omega_3}^{V_2} & 0 & 0 & 0 & M_{\Omega_3} \end{bmatrix} \begin{Bmatrix} \dot{V}_1 \\ \dot{V}_2 \\ \dot{V}_3 \\ \dot{\Omega}_1 \\ \dot{\Omega}_2 \\ \dot{\Omega}_3 \end{Bmatrix} = \begin{Bmatrix} \mathrm{RHS}_{V_1} \\ \mathrm{RHS}_{V_2} \\ \mathrm{RHS}_{V_3} \\ \mathrm{RHS}_{\Omega_1} \\ \mathrm{RHS}_{\Omega_2} \\ \mathrm{RHS}_{\Omega_3} \end{Bmatrix}$$

$$\begin{bmatrix} M_{\gamma_1} & 0 & 0 & 0 & 0 & 0 \\ 0 & M_{\gamma_2} & 0 & 0 & 0 & 0 \\ 0 & 0 & M_{\gamma_3} & 0 & 0 & 0 \\ 0 & 0 & 0 & M_{\kappa_1} & 0 & 0 \\ 0 & 0 & 0 & 0 & M_{\kappa_2} & 0 \\ 0 & 0 & 0 & 0 & 0 & M_{\kappa_3} \end{bmatrix} \begin{Bmatrix} \dot{\gamma}_1 \\ \dot{\gamma}_2 \\ \dot{\gamma}_3 \\ \dot{\kappa}_1 \\ \dot{\kappa}_2 \\ \dot{\kappa}_3 \end{Bmatrix} = \begin{Bmatrix} \mathrm{RHS}_{\gamma_1} \\ \mathrm{RHS}_{\gamma_2} \\ \mathrm{RHS}_{\gamma_3} \\ \mathrm{RHS}_{\kappa_1} \\ \mathrm{RHS}_{\kappa_2} \\ \mathrm{RHS}_{\kappa_3} \end{Bmatrix} \tag{6}$$

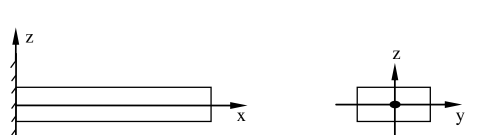

Fig. 1 Definition of the b-system for an undeformed cantilever beam.

where M_{V_1}, $M_{V_1}^{\Omega_2}$, etc., are the mass matrices in FEM, and RHS stands for the right-hand side, including all the nonlinear terms. Combining all the ODEs, we obtain the following concisely denoted form:

$$\frac{\mathrm{d}}{\mathrm{d}t}\{q\} = \{g\} \tag{7}$$

where $\{q\}$ consists of all the nodal values of variables; each node has 18 degrees of freedom, including velocities, angular velocities, internal strain, internal curvature, displacements, and Rodrigues parameters; and the right-hand side $\{g\}$ is a function of $\{q\}$ and time t. Detailed development of the above FEM discretization and how to obtain the RHSs and the validation of our FEM approach can be seen in [11].

A second-order implicit method is used for time integration:

$$\{q\}_{k+1} = \{q\}_k + \left(\Delta - \alpha\Delta t \frac{\partial g}{\partial q}\bigg|_{q_k}\right)^{-1} \Delta t[(1-\alpha)\{g(t_k, q_k)\} + \alpha\{g(t_{k+1}, q_k)\}] \tag{8}$$

where Δ is the identity matrix; subscript $k+1$ denotes values at time t_{k+1}, and subscript k denotes those at time t_k; Δt is the time-step size; and α is a real factor between 0.5 and 1.0, usually chosen to be 0.5. Note that in evaluation of $g(t_k, q_k)$ and $g(t_{k+1}, q_k)$, the time t_k and t_{k+1} will be explicitly indicated by the wake solutions of the present aerodynamic solver, UVLM, which will be introduced in the following.

The main task of programming would be providing a subroutine or function to calculate the column vector $\{g\}$ as a function of time t and $\{q\}$. To solve for $\{q\}_{k+1}$ from Eq. (8), we need to evaluate the Jacobian matrix $\partial g/\partial q$; it can only be numerically computed.

III. Nonlinear Aerodynamic Model: Unsteady Vortex-Lattice Method

A. Description of UVLM

The UVLM [12–14] employed here solves for incompressible unsteady aerodynamics over a flexible thin wing with its shed free wake in the time domain. The thin-wing surface is represented by a sheet of distributed vorticities for which the strengths together with those of the wake sheet vorticities are solved simultaneously at each time step. The vortices are lined up in a lattice or finite-element-like format (see Fig. 2): hence, the vortex-lattice method. Unlike the previous vortex-lattice method or the doublet-lattice method, the present vortex-lattice method adopts a nonlinear flow modeling.

For element i in Fig. 2, the value of the loop circulation is denoted by G_i. The circulation around a given segment is obtained by taking all the adjoining loops into account, all of which have the given segment in common. For example, in Fig. 2, the circulation around segment j of the loop that encircles element i is given by

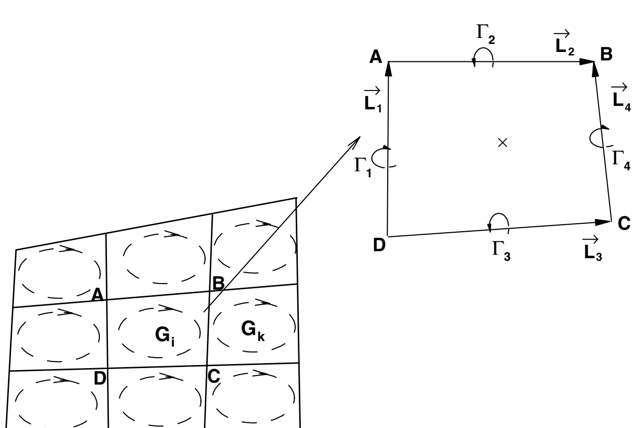

Fig. 2 Vortex lattice.

$$\Gamma_{ij} = G_k - G_i \tag{9}$$

The velocity associated with each segment in the vortex-lattice is calculated by the well-known Biot–Savart law; hence, the calculated velocity field away from the vortex sheets is both irrotational and incompressible and decays with distance. It is well known that there is a singularity issue with Biot–Savart law. The issue has been circumvented by assuming there is a viscous core around the vortex segment. Currently, Mook's method is used, i.e., within the cutoff radius of the vortex segment, the induced velocity equals zero. There are also some other methods available, e.g., Lamb's, Schlinker's, and McCroskey's models.

B. No-Penetration Condition

In the actual flowfield, the velocity associated with the vorticity satisfies the no-penetration and no-slip boundary conditions on the surface of the body. Imitating real life, we determine the distribution of vorticity in the lattice by requiring the normal component of the velocity of the air relative to the moving surface of the wing to vanish at the control points of the elements of the lattice; these are located at the centroids of the elements:

$$\sum_{j=1}^{M} A_{ij} G_j = (\mathbf{v}_{\text{surface}} - \mathbf{v}_{\text{wake}} - \mathbf{v}_{\text{freestream}}) \cdot \mathbf{n}_i \tag{10}$$

for $i = 1, 2, \ldots, M$, where M is the number of elements in the aerodynamic grid; A_{ij} is the normal component of the velocity at the control point of element i associated with a closed, generally nonplanar, loop of unit-circulation vortex segments around the edges of element j; G_j is the actual circulation around the vortex segments enclosing element j; $\mathbf{v}_{\text{surface}}$ is the velocity of the control point of element i on the deforming camber surface; $\mathbf{v}_{\text{wake}}$ is the velocity at the control point of element i associated with the vorticity in the wake (the wake is discussed below); $\mathbf{v}_{\text{freestream}}$ is the velocity of freestream or the wind; and $\mathbf{n}_i$ is the unit vector normal to the surface of element i (obtained from the cross product of the diagonals). When the wing is deforming, the relative positions of the aerodynamic nodes are changing with time; hence, A_{ij} and $\mathbf{n}_i$ are also changing and must be recomputed at each time step.

C. Wake Formation by Vorticity Shedding and Convecting

The Kutta condition is imposed by shedding vorticity from the lines of flow separation into the wake, and the wake is formed by convecting the vortex segments there with the local particle velocity while holding the circulations around them constant. The shedding–convecting process generates the vortex lattice that represents the wake as part of the solution.

At each time step, new vortices are formed, shed, and convected away from the edges to form the wake. It is clear that the wake stores the history of the circulation strength in those vortex elements in which the wake is shed. We say that the wake is the historian of the flow. From the Biot–Savart law, the velocity is inversely proportional to the distance of the field point away from the vortex filament, and so the wake vortices that are far from the wing or the body have negligible effects on the wing or the body. In numerical applications, we can safely cut off those wake vortices. In practice, we give a fixed maximum number for the rows of the wake. Those wake vortices that are far downstream are neglected (in the future, we might instead consider an analytical approximation for the far-field wake contribution). This shedding and convecting process can simulate the rolling up of the tip vortices, which is demonstrated in Fig. 3 for a small-aspect-ratio rectangular wing.

The updating of the wake position at each moment is obviously the most time-consuming part in the present UVLM method. However, the use of parallel computation can greatly mitigate this issue. One could choose either openMP or message-passing interface approaches to facilitate parallel computation, depending on the computer planform. Both methods have been implemented in the current paper to expedite UVLM.

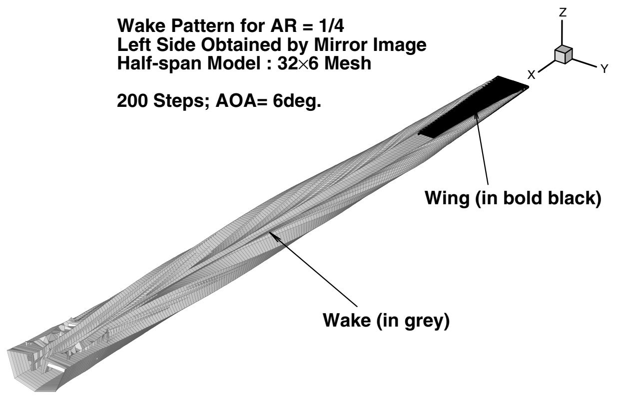

Fig. 3 Illustration of rolling-up vortices from a small-aspect-ratio rectangular wing.

IV. Discrete-Gust Implementation

Discrete-gust analysis has typically relied on frequency-domain analysis first, then used the rational function approximation method or inverse Fourier transformation to extract time-domain solution for ASE analysis [2,3]. In this paper, the gust implementation is very straightforward in the time-domain aerodynamic model employed here: namely, the general UVLM. The effects of gust on the trailing wake are well captured, as we will show later.

For a traveling gust with an arbitrary profile, its transverse velocity component (with respect to the far-field freestream velocity) time-domain representation is illustrated in Fig. 4 and expressed as a gust magnitude multiplied by a time function T in Eq. (11):

$$\bar{V}_G = V_G T\left(t - \frac{x - x_o}{V}\right) \tag{11}$$

where t is time, x_0 is the reference point for the gust, V is the freestream speed, x is a point on the aircraft, and V_G is the magnitude of the gust.

For a one-minus-cosine gust, its equivalent form of Eq. (11) can be expressed as

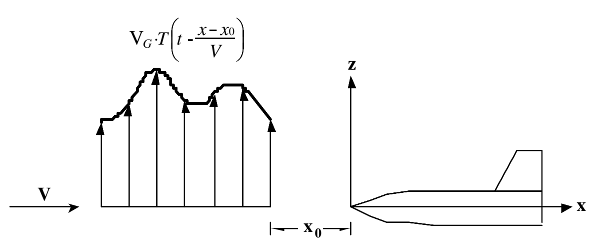

Fig. 4 Time-domain representation of a traveling gust with an arbitrary profile.

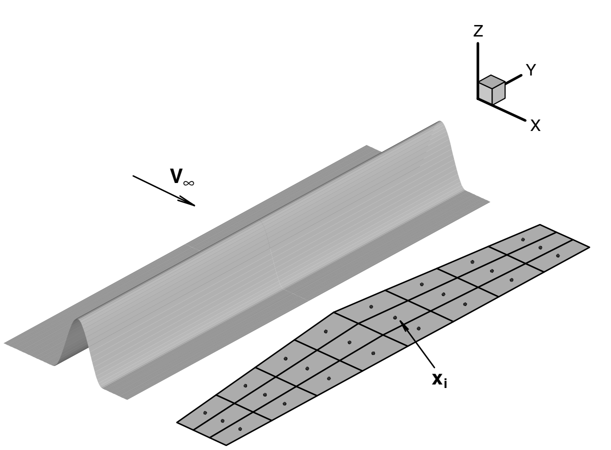

Fig. 5 Implementation of gust effects in UVLM.

$$\bar{V}_G(x, t) = \begin{cases} \frac{1}{2} V_G\left(1 - \cos\frac{2\pi\tau}{L_G/V}\right) & \text{for } 0 \le \tau \le L_G/V \\ 0 & \text{for } \tau > L_G/V \text{ or } \tau < 0 \end{cases} \tag{12}$$

where $\tau = t - [(x - x_o)/V]$, and L_G is the length of the gust profile.

Numerical implementation of the gust effects due to a traveling one-minus-cosine gust profile into our nonlinear-structure/nonlinear-aerodynamics methodology is illustrated in Fig. 5. The shaded profile represents a traveling gust. The gust is assumed to be uniform along the spanwise direction and only has a vertical component. For a given time t, the flow velocity due to gust at a control point, x_i, can be immediately calculated using Eq. (12). This component is then added into the boundary condition of the UVLM model to satisfy the no-penetration condition at the aerodynamic panels:

$$\sum_{j=1}^{M} A_{ij} G_j = (\mathbf{v}_{\text{surface}}\text{-}\mathbf{v}_{\text{wake}}\text{-}\mathbf{v}_{\text{freestream}}\text{-}\mathbf{v}_{\text{gust}}) \cdot \mathbf{n}_i \tag{13}$$

The boundary condition is not only modified for the presence of the gust, but the convection of the wake should also take into account the effects of the gust, i.e., when calculating the convecting velocity of the wake element (the local fluid particle velocity), the contributions from the gust are added in as well.

V. Numerical Results for a HALE Wing Under Discrete Gust

A. Gust Analysis Validation Through a Goland Wing

Before applying the gust analysis to a HALE wing, we validate the methodology on a rather stiff wing model, a Goland wing, for which the geometry and properties can be found in [11]. Our solution is compared with the solution of ZAERO [15].

The rigid wing at zero angle of attack is first considered. Figure 6a shows the time history of the gust velocity at the origin of the coordinate system (the quarter-chord position from the leading edge). The discrete-gust profile is as follows: $V_G/V = 0.001$ and $L_G = 4$ chord length. The mean freestream speed is chosen to be $100\ \mathrm{m/s}$. The strength of this chosen gust profile is small, so that the aerodynamics will be in the linear domain, and thus allows us to compare it with the solutions by the linear aerodynamic model. The time histories of the total lift coefficient are given in Fig. 6b. For comparison, the lift-coefficient solution by ZAERO is plotted in the same figure. We can see that the current gust analysis by UVLM agrees very well with ZAERO.

Figure 7 shows several snapshots of the elastic Goland wing and its wake (only the right half is shown) under the same gust profile as the rigid-wing case and at zero angle of attack, but the mean freestream speed is $100\ \mathrm{m/s}$ as well. After the gust passes the wing, its effects are still captured by the motion of the trailing wake and consequently affect the aerodynamic loading on the wing. The tip deflection and twist of the Goland wing are given in Fig. 8. It can be seen that the solutions obtained by the present nonlinear code agree well with those by ZAERO. It should be noted that the intrinsic structural model employed here does not use the twist angle as a primary variable. It can only be solved from the transformation matrix and through the Euler angles. One may have different ways to apply the Euler angle sequence (e.g., 1-2-3, 3-2-1). For the small-deformation case in this example, the choice of the sequence should not have much effect. Also noteworthy is that ZAERO conducts the gust analysis in the frequency domain first, then performs an inverse Fourier transformation or rational function approximation to get the time-domain solution.

B. Gust Analysis for a HALE Wing

The same HALE wing analyzed in [16] is considered again here. Its geometry is repeated in Fig. 9a, and the aerodynamic grids of the undeformed configuration and one typical deformed configuration are shown in Fig. 9b. It has a span of 238.8 ft (72.78 m) and a constant chord of 8 ft (2.44 m). At each end, there is a 10 deg dihedral angle. The inertial and elastic properties of the wing's cross section are given in Table 1.

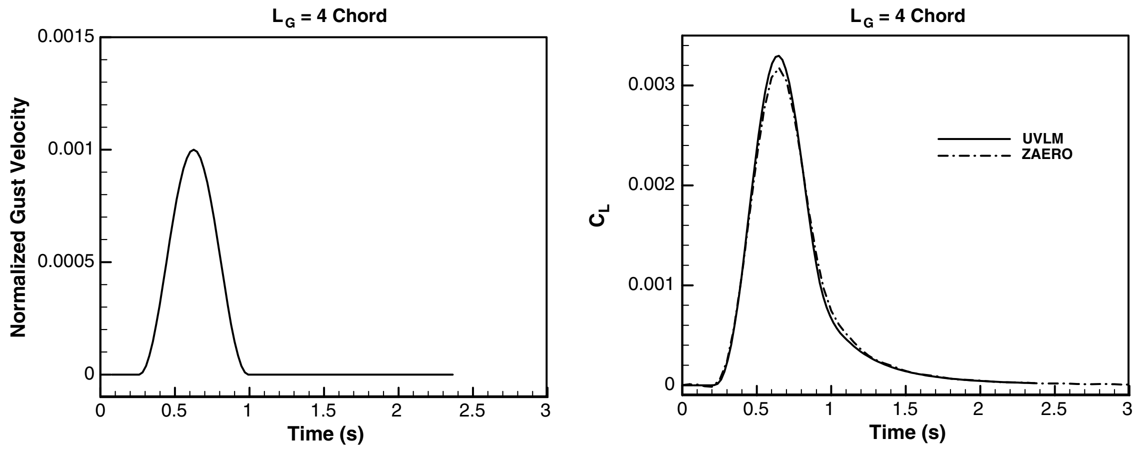

a) b)

Fig. 6 Plots of a) time history of the gust velocity at the origin of the coordinate system and b) comparison of solutions for the total lift coefficient vs time under the gust.

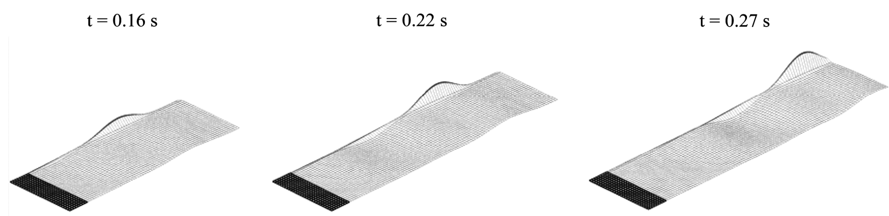

Fig. 7 Snapshots of the deformed Goland wing and its wake with a traveling gust ($V_G/V = 0.001$, $L_G = 4$ chord length, and $V = 100$ m/s).

In the time-domain simulation, only one-half of the wing is analyzed and modeled as a cantilever beam, and the aerodynamic symmetry about the center plane is taken into account. The elastic axis of the wing is at the 25% chord from the leading edge, and the mass center of the cross sections is assumed to be coincident with the elastic center. Air density is chosen to be 1.229 kg/m^3, which corresponds to the one at sea level. The pods, which are located at two-thirds of the semispan distance from the midspan, weigh 50 lb each and are modeled as point-concentrated masses in the structural model. The central pod acts as a bay for payload and weighs 560 lb when it is fully loaded.

Before the gust analysis, the responses of the HALE wing under various angles of attack are analyzed. The simulation starts from zero initial conditions. The wing is impulsively started from its undeformed configuration. It is expected that when the angle of attack is not high enough, solutions will approach a steady state. The trim angle of attack, under which the lift balances the total weight of the wing, is found to be around 5.89 deg for the rigid wing and 6.5 deg for the flexible wing, compared with ZAERO's solutions of 6.0 deg for the rigid wing and 7.0 deg for the flexible wing. The trim solutions are presented in Table 2. Also shown in Table 2 is the Patil and Hodges [16] solution of 30 ft, and as a side note, the averaged Helios flight-test-measured wing dihedral [1] is around 15 ft. However, note that the Helios prototype aircraft has different geometry and structural properties from the presented HALE-wing model.

The time histories of tip deflections for the wing at various angles of attack are given in Fig. 10. Gravity is included in the simulation. At an angle of attack (AoA) below 10 deg, the tip deflections approach steady solutions. At 12 deg angle of attack, periodic solutions are observed; above this angle of attack, the solutions become chaotic. At 16 deg AoA, large oscillatory motion occurs with a rather small frequency close to 0.2 Hz. When time t is under 28 s, the deformation of the HALE-wing model increases monotonically and no oscillation is detected. However, beyond $t = 28$ s, where the wing deformation increases to a threshold value, a large oscillatory motion appears that may lead to a structural failure. This result obtained by NANSI

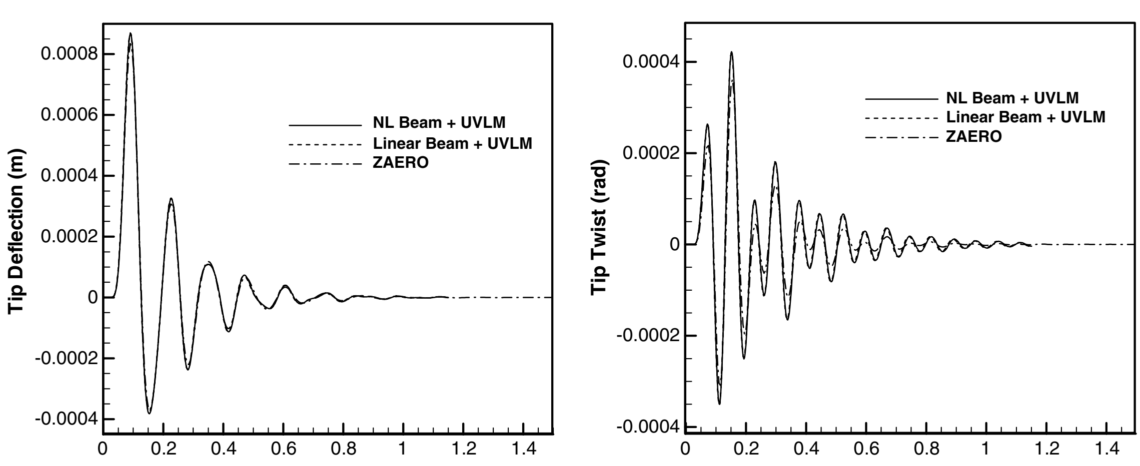

Fig. 8 Elastic Goland wing responses subject to a traveling gust ($V_G/V = 0.001$, $L_G = 4$ chord length, and $V = 100$ m/s).

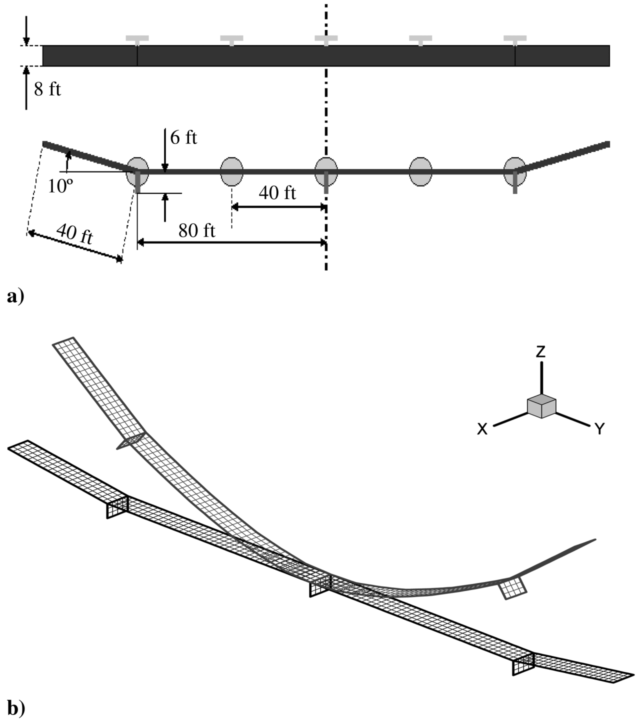

Fig. 9 Illustrations of a) geometry of the HALE-wing model and b) aerodynamic grid of the undeformed/deformed HALE-wing model.

indicates that the aeroelastic stability of the HALE wing depends on its deformed shape. At small or moderate deformation, the HALE wing is aeroelastically stable but becomes unstable when it has a large deformed shape.

As mentioned above, the HALE wing achieves trim condition at about 6.5 deg of angle of attack and 40 ft/s flight speed. Under this trim condition, the HALE wing is then analyzed subject to various gust profiles. In the time-domain solution procedure, the trim solution is first obtained, then followed by the gust applications. Figure 11 presents the tip deformations at $V_G = 20$ ft/s and various gust profile length ranging from 15 to 30 chord lengths, and Fig. 12 gives the solutions at $L_G = 25$ chord length and various gust velocity magnitudes ranging from 10 to 25 ft/s. It is found from these two plots that under certain levels of gust, the elastic deformations of the HALE wing tend to become unstable; notably, the in-plane deflections become significantly large. Below the critical-gust condition, the HALE wing will approach a stable solution after passing the gust profile. Figure 13 presents several typical responses of the deformed HALE wing and its wake as the gust passes through. The effects on the trailing wake of the passing of the wake can be clearly seen from the sequences of plots.

At this stage, we note that the previous consideration of the HALE-wing instability may well be subjected to flow separation caused by high wind incidences (AoA) as well as wind gust. In turn, the separated flow could induce local wing stall and/or wing twist. The next section will present an engineering methodology to account for wing stall effects.

Table 1 HALE-wing properties

Item	Value
Torsional rigidity	0.4×10^6 lb/ft^2 = 1.65301×10^5 Nm^2
Bending rigidity	2.5×10^6 lb/ ft^2 = 1.03313×10^6 Nm^2
Bending rigidity (chordwise)	30×10^6 lb/ft^2 = 1.23976×10^7 Nm^2
mass per unit length	6 lb/ft = 8.92898 kg/m
Centroidal mass moment of inertia about the x axis (Torsional)	30 lb/ft = 4.14765 kg/m
Centroidal mass moment of inertia about the y axis	5 lb/ft = 0.691275 kg/m
Centroidal mass moment of inertia about the z axis	25 lb/ft = 3.45637 kg/m

Table 2 Comparison of trim solutions

Trim solutions	Present (NANSI)	ZAERO	Patil/Hodges [16]
AoA	6.5 deg.	7 deg.	5 deg.
Wing dihedral	18 ft	20 ft	30 ft

VI. Unsteady Aerodynamic Loads at and Beyond Stall

A. Methodology

UVLM has demonstrated successful prediction of the aerodynamic lift for small to moderate angles of attack [11,17]. In the range of stall in which the flow separation dictates the aerodynamics, it is desirable for the aerodynamic model to capture such stall characteristics. Attacking the flow separation in the three-dimensional case proves to be very complicated; most existing post-stall prediction methodologies use the two-dimensional section data. The use of sectional data enables us to bypass the modeling of various kinds of flow-separation phenomena, which include laminar separation bubble, turbulent reattachment, leading-edge stall, etc.

In this paper, an engineering approach is investigated by coupling the three-dimensional UVLM with the known two-dimensional section data for predicting the aerodynamic characteristics of a finite wing near and beyond stall. The present approach is based on the strip assumption, and so its use has been constrained to large-aspect-ratio wings, for which sectional flow velocities along the spanwise direction are relatively small. For HALE-wing applications, this condition is clearly applicable. It is considered that this assumption is good enough for a first-order theory. Under such an assumption, the sectional lift of the wing is directly related to the effective angle of attack. Before stall, the sectional lift is proportional to the effective angle of attack. Beyond stall, the sectional lift exhibits a nonlinear relationship with the effective angle of attack.

Incorporating the concept of the effective angle of attack, we adopt UVLM as a basis aerodynamic model. Thus, our task is to add one additional nonlinear separated-flow feature to UVLM. But such a task is by no means trivial. Several basic features of UVLM are revisited first. We note that the nonlinearity of UVLM lies in three places: 1) flow tangency conditions applied on an updated surface (similar to the follower force effect), 2) free wake, and 3) viscous effect modeled by vortex dynamics. Thus, the separated-flow model of UVLM would allow a physical modeling similar to the one that we established previously in an unsteady transonic lifting-surface method [18], also known as the transonic-equivalent-strip (TES) method. Following the TES concept, one assumes that the potential solutions are separable. Thus,

$$\Phi(x, y, z, t) = \Phi_0(x, z, t)\Psi(y, t) \tag{14}$$

Accordingly, it can be shown that the relation between ΔC_{p3}^N and ΔC_{p2}^N holds:

$$\Delta C_{p3}^N = \Delta C_{p2}^N \mathbf{F}_n(\Delta C_{p3}^V, \Delta C_{p2}^V) \tag{15}$$

where superscript N denotes the general flow nonlinearities, including that of UVLM and flow-separation effect, and superscript V denotes UVLM flow nonlinearity with only vortex roll-up and free-wake effects. ΔC_{p3} and ΔC_{p2} denote the 3-D and 2-D pressure differential (or lifting pressure) across the wing planform, respectively. Equation (15) can be also integrated to yield a sectional-lift relation:

$$C_{\ell 3}^N = C_{\ell 2}^N \mathbf{G}_n(C_{\ell 3}^V, C_{\ell 2}^V) \tag{16}$$

The functions $\mathbf{F}_n$ and $\mathbf{G}_n$ are equivalent-strip functions derived by the similarity concept. Thus, given 2-D nonlinear flow C_p and/or C_ℓ by measured data or by computed solution (e.g., UVLM 2-D or

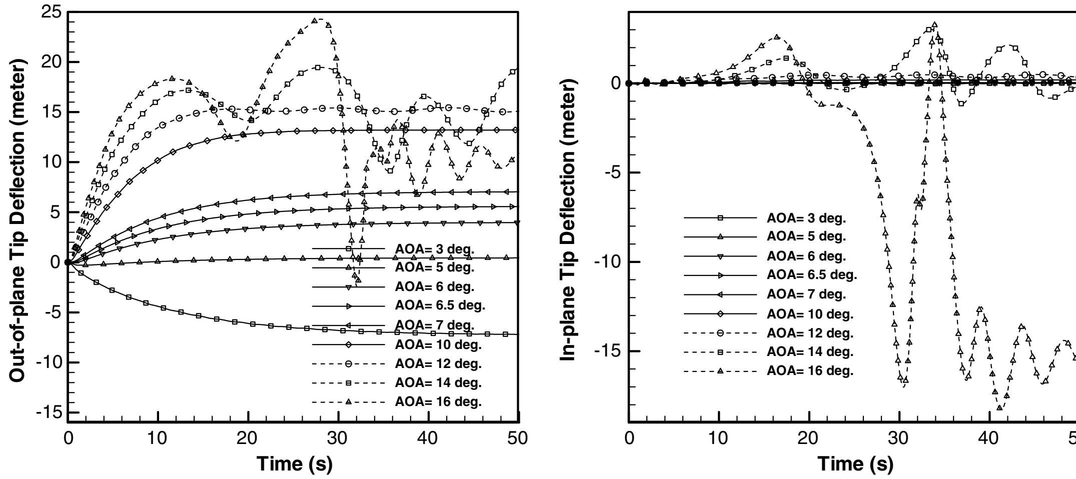

Fig. 10 Time histories of tip deflections at various angles of attack for the HALE wing (without gust).

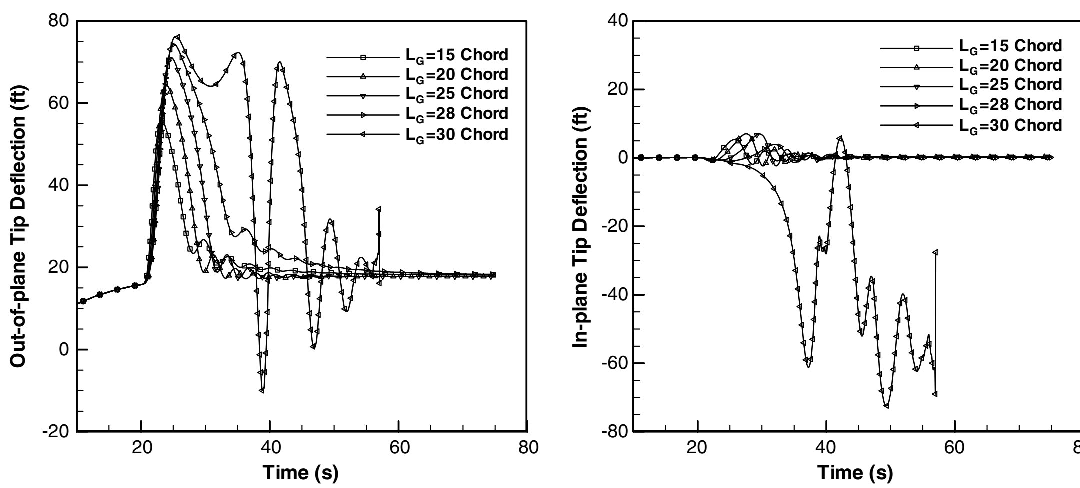

Fig. 11 HALE-wing response at 1 *g* trim angle of attack and under gust with varying profile length ($V_G = 20$ ft/s).

XFOIL [19]) along with our supplied 3-D solutions by UVLM, the 3-D lifting pressure and spanwise lift distribution can be obtained through Eqs. (15) and (16).

Note that the formulas established in Eqs. (15) and (16) hold for steady and unsteady lifting pressures and lift forces. The computation procedure (denoted as UVLM/stall) can be described as follows. Based on the lifting-line concept, the effective angle of attack at each section is computed by

$$\alpha_{\mathrm{eff}_i} = \frac{c_{li}^V}{c_{l\alpha}} + \alpha_0 \quad \text{where } i = 1, 2, \ldots, n \tag{17}$$

where C_{li}^V is the sectional lift by UVLM, $c_{l\alpha}$ is the slope of the linear part of the known 2-D lift curve (e.g., [20]), and α_0 is the 2-D zero-lift angle of attack. In Eqs. (15) and (16), 2-D pressure ΔC_{p2}^N and sectional lift C_{l2}^V are computed at the effective angle of attack, which

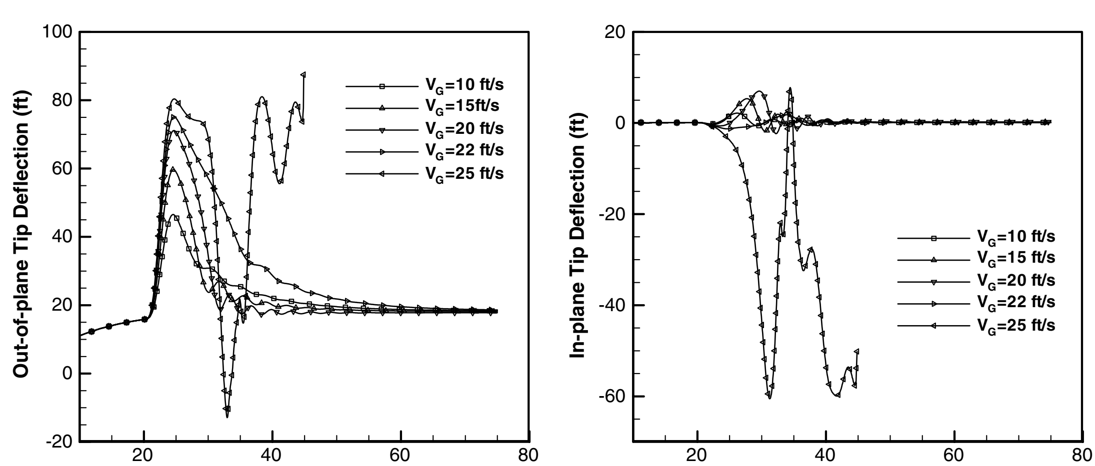

Fig. 12 HALE-wing response at 1 *g* trim angle of attack and under gust with varying magnitude ($L_G = 25$ chord length).

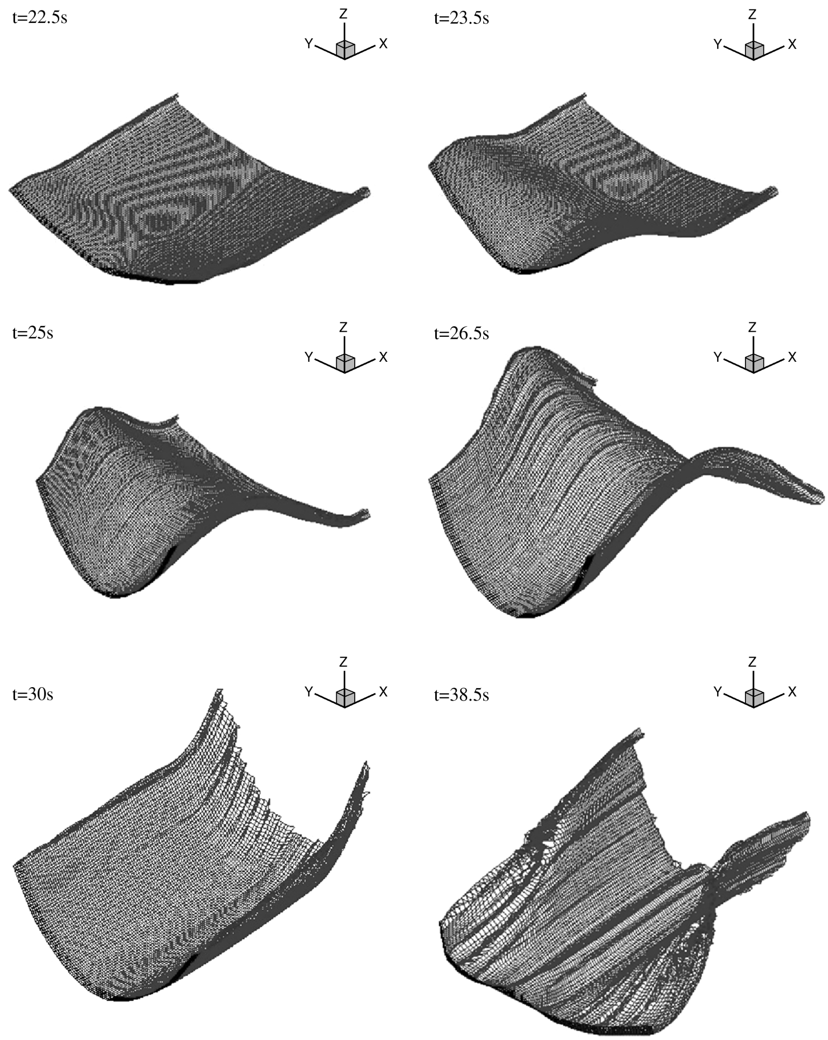

Fig. 13 Snapshots of the deformed HALE wing and the wake when a gust is passing through ($V_G = 20$ ft/s, $L_G = 30$ chord length).

can be obtained through existing codes such as XFOIL [19] or supplied by measured data; 2-D pressure ΔC^V_{p2} is also computed at the effective angle of attack and is obtained by the corresponding 2-D UVLM method. Note that ΔC^N_{p2} and ΔC^V_{p2} chordwise distribution can be computed at a series of angles of attack beforehand. For intermediate angles of attack, the distribution will be obtained by using the spline interpolation technique. Similarly, spline interpolation on the chordwise locations may also be needed, because ΔC^N_{p2}, ΔC^V_{p2}, and ΔC^V_{p3} may be computed at different chordwise locations for each strip or section.

Supposedly, should an appropriate sectional ΔC^N_{p2} be provided, the present stall model would be applicable to a wide range of Reynolds number flows, from those for large-scale aircraft to those for micro air vehicles.

B. Numerical Results for Stall Modeling

To verify the above procedure, an aspect-ratio-6 rectangular wing with NACA0012 airfoil is analyzed as a numerical example before we apply the procedure to NANSI.

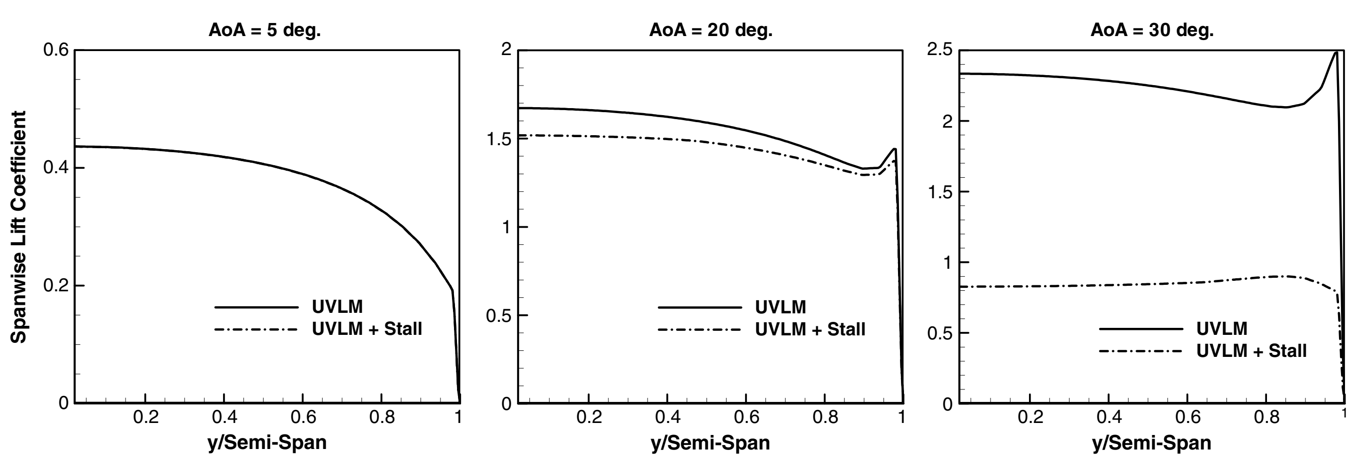

Fig. 14 Comparison of UVLM and UVLM/Stall solutions: Spanwise lift distributions of a rectangle wing with NACA 0012 airfoil section (AR = 6, and AOA = 5, 20, 30 deg.).

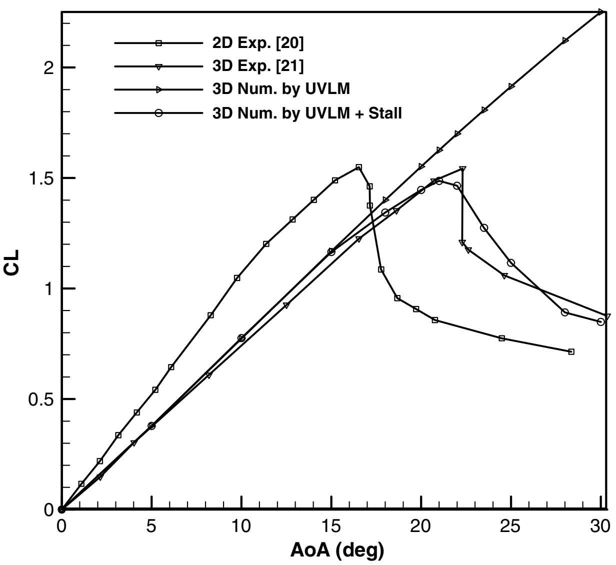

Fig. 15 Lift curve for a rectangle wing (AR = 6) with NACA 0012 airfoil section.

Figure 14 presents the spanwise lift distribution solutions for the rectangular wing at three different angles of attack. At low angles of attack, the lift distribution does not require flow-separation correction; at medium angles of attack, flow-separation effects kick in; and at large angles of attack, significant lift drop is obtained due to stall effects. Figure 15 shows the total lift vs angle of attack. To validate UVLM/stall, we compare the results of the computed total lift with that measured data from [21]. It can be seen from Fig. 15 that the UVLM/stall solution correlates favorably with the measured data throughout the angle-of-attack range extending beyond stall.

In Figs. 16 and 17 we present the comparison for the solutions with or without consideration of stall for the HALE-wing example analyzed in Sec. V. The cross-sectional profile for this HALE wing is also assumed to be NACA0012. The flight speed is the same as 40 ft/s. Figure 16 shows the solutions without gust present and under two different angles of attack: 6.5 and 16 deg. Recall that the trim angle for the HALE wing is 6.5 deg. As expected, the tip deflections are essentially the same for UVLM and UVLM/stall correction when the angle of attack is 6.5 deg. At 6.5 deg, the effective angle of attack at each section does not approach the stall range, and thus no correction is necessary. At 16 deg angle of attack, instabilities for the HALE wing are observed with or without considering stall effects. The inclusion of stall effects seems to accelerate the occurrence of the instability of in-plane deflection.

Figure 17 shows the solution of the HALE wing under a discrete gust with $V_G = 20$ ft/s and $L_G = 30$ chord length. Again, the inclusion of stall correction does not greatly affect the instability of the HALE wing's responses under such an intensive gust profile. The instability associated with the in-plane deflection appears earlier when stall or flow separation is considered, compared with the case without such stall corrections.

Figure 18 presents the side-by-side comparison of the wake without or with stall consideration (or the stall model). The no-stall

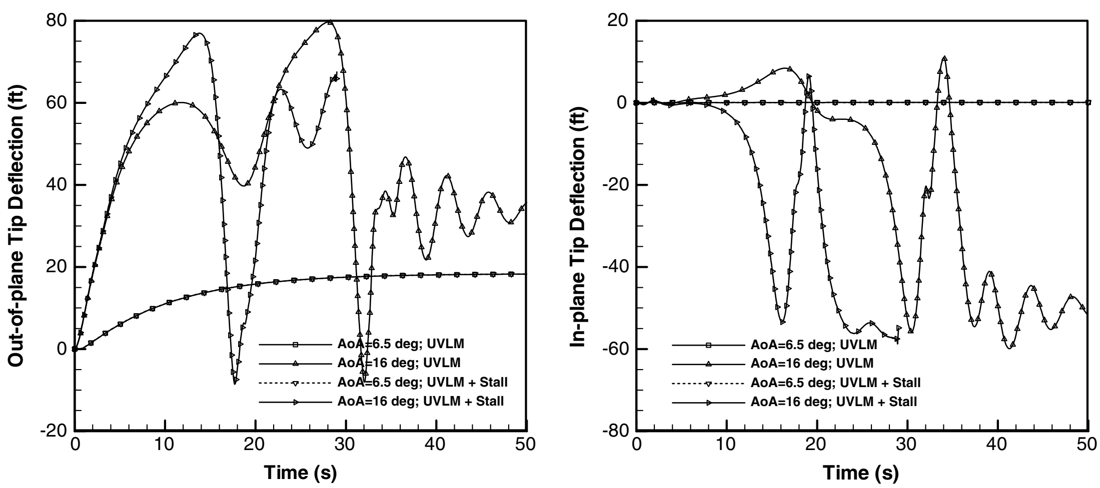

Fig. 16 HALE-wing responses by UVLM with and without stall consideration (No Gust).

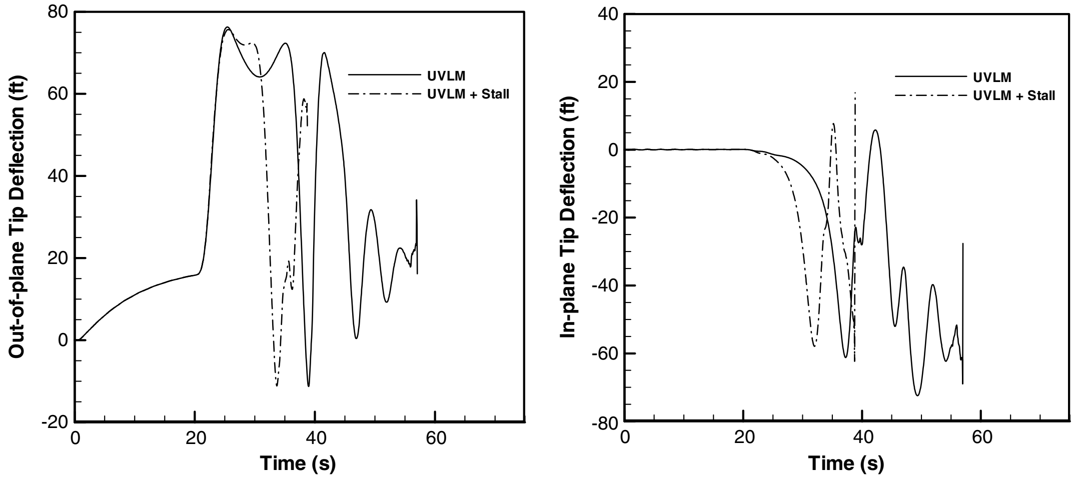

Fig. 17 HALE-wing responses by UVLM with and without stall consideration under gust ($V_G = 20$ ft/s and $L_G = 30$ chord length).

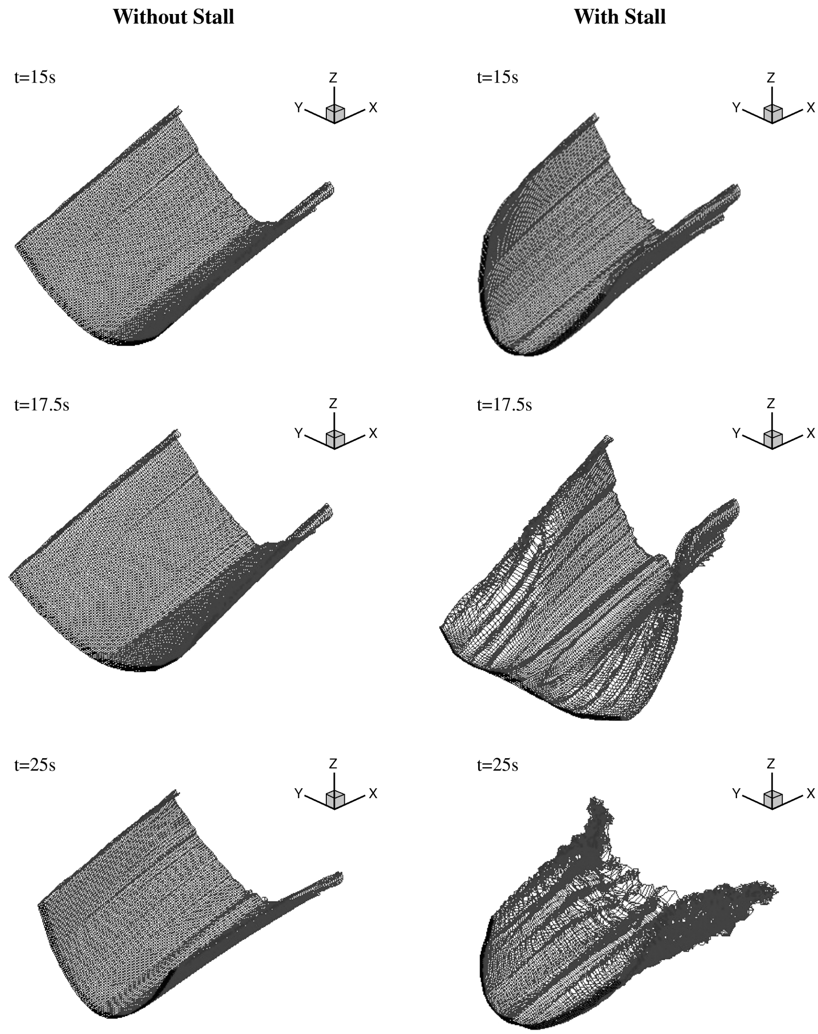

Fig. 18 Side-by-side comparison of the wake without and with stall consideration (no gusts, AoA is 16 deg, and $V_C = 40$ ft/s).

model tends to maintain the organized vortex roll-up into the wake sheet. By contrast, the large effects due to the stall model on the wing deformations and the early breakdown of the vortex roll-up into the wake are clearly seen.

When stall effects are considered, the code stopped in the time-marching process after the occurrence of in-plane instability. A possible cause could be due to the chaotic convecting of the trailing wake related to the large structural deformations; thereafter, the time-marching algorithm becomes unstable. There is no doubt that further investigation and validation of the above procedure to consider flow separation or stall effects are necessary.

VII. Conclusions

Our method of nonlinear-aerodynamics/nonlinear-structure interactions (NANSI), a tightly coupling of UVLM with a nonlinear beam model, is enhanced to include the capability of handling gust and stall flow for a high-aspect-ratio HALE wing.

We have examined three advanced models of NANSI: namely, with gust alone, with stall flow alone, and with both. First, the one-minus-cosine gust model has been verified and studied extensively. For the HALE wing at 1 g trim, critical-gust profile length and gust magnitude are identified at 30 chord lengths and 25 ft/s, respectively. Next, a stall-flow model based on the lifting-line concept employing an equivalent-strip procedure is developed to account for the HALE wing at flow conditions of stall and beyond. It is found that NANSI with stall flow would not alter the previous state of critical AoA when the HALE is only subject to vortex roll-up without the participation of a stall-flow model. However, critical-failure (aeroelastic instability) time (when significant in-plane deflection occurs) by NANSI/stall is found to be nearly half of the failure time by NANSI without stall (i.e., 18 s versus 32 s at the critical AoA of 16 deg). This can be justified by observing the simulated snapshots in Fig. 18. It is believed that the stall model is responsible for the early breakdown of the vortex roll-up promoting the unorganized vortical dynamics and hence moves up the failure time.

When the HALE wing is subject to wing gust and stall flow combined, the critical-failure time would be somehow delayed and comparable with that due to gust alone. For all cases considered, the critical wing-tip deflection would invariantly reach nearly two-thirds of the wing semispan, which might indicate that the wing failure is related to its large dihedral. At small or moderate deformations, the HALE wing tends to be aeroelastically stable but becomes unstable at large deformed shapes. The physical reason for these findings is not entirely clear at present. Further numerical studies and wind-tunnel tests are warranted.

Further improvements of the present NANSI method are twofold. It is important to incorporate the random-gust model and to develop means to allocate the three-dimensional separation line for the NANSI/stall model. As opposed to the time-domain CFD methods, the present enhanced NANSI method should be an effective solver applicable to wings for large-sized aircraft. The stall model developed should be applicable in almost all ranges of Reynolds number flows, including that for the micro air vehicles.

References

[1] Noll, T. E., Brown, J. M., Perez-Davis, M. E., Ishmael, S. D., Tiffany, G. C., and Gaier, M., "Investigation of the Helios Prototype Aircraft

Mishap—Volume 1: Mishap Report," NASA, 2004.

[2] Chen, P. C., "Nonhomogeneous State-Space Approach for Discrete Gust Analysis of Open-Loop/Closed-Loop Aeroelastic Systems," AIAA Paper 2002-1715, 2002.

[3] Karpel, M., Moulin, B., and Chen, P. C., "Dynamic Response of Aeroservoelastic Systems to Gust Excitation," *Journal of Aircraft*, Vol. 42, No. 5, 2005, pp. 1264–1272. doi:10.2514/1.6678

[4] Raveh, D. E., "CFD-Based Models of Aerodynamic Gust Response," AIAA Paper 2006-2022, 2006.

[5] Schairer, R. S., "Unsymmetrical Lift Distributions on a Stalled Monoplane Wing," Ph.D. Thesis, California Inst. of Technology, Pasadena, CA, 1939.

[6] Levinsky, E. S., "Theory of Wing Span Loading Instabilities Near Stall," AGARD Conference Proceedings, CP 204, AGARD Paper 25, 1976.

[7] van Dam, C. P., Vander Kam, J. C., and Paris, J. K., "Design-Oriented High-Lift Methodology for General Aviation and Civil Transport Aircraft," *Journal of Aircraft*, Vol. 38, No. 6, 2001, pp. 1076–1084. doi:10.2514/2.2875

[8] Tani, I., "A Simple Method of Calculating the Induced Velocity of a Monoplane Wing," Aeronautical Research Inst., Tokyo Imperial Univ., Rept. 111, Tokyo, 1934.

[9] Mukherjee, R., Gopalarathnam, A., and Kim, S., "An Iterative Decambering Approach for Post-Stall Prediction of Wing Characteristics Using Known Section Data," AIAA Paper 2003-1097, 2003.

[10] Hodges, D. H., "Geometrically Exact, Intrinsic Theory for Dynamics of Curved and Twisted Anisotropic Beams," *AIAA Journal*, Vol. 41, No. 6, 2003, pp. 1131–1137. doi:10.2514/2.2054

[11] Wang, Z., Chen, P. C., Liu, D. D., Mook, D. T., and Patil, M. J., "Time-Domain Nonlinear Aeroelastic Analysis for HALE Wings," AIAA Paper 2006-1640, 2006.

[12] Mook, D. T., and Nayfeh, A. H., "Numerical Simulations of Dynamic/Aerodynamic Interactions," *Computing Systems in Engineering*, Vol. 1, Nos. 2–4, 1990, pp. 461–482. doi:10.1016/0956-0521(90)90030-O

[13] Wang, Z., Magill, S., Preidikman, S., Mook, D., and Schetz, J., "A Numerical and Experimental Aerodynamic Analysis of an Inboard-Wing/Twin-Fuselage Configuration," AIAA Paper 2001-2431, 2001.

[14] Preidikman, S., and Mook, D. T., "Time-Domain Simulation of Linear and Nonlinear Aeroelastic Behavior," *Journal of Vibration and Control*, Vol. 6, No. 8, 2000, pp. 1135–1175. doi:10.1177/107754630000600802

[15] *ZAERO User's Manual*, ZONA Technology, Inc., Scottsdale, AZ, 2003.

[16] Patil, M. J., and Hodges, D. H., "Flight Dynamics of Highly Flexible Flying Wings," *Proceedings of the International Forum on Aeroelasticity and Structural Dynamics*, Munich, Germany, June 2005.

[17] Wang, Z., "Time-Domain Simulations of Aerodynamic Forces on Three-Dimensional Configurations, Unstable Aeroelastic Responses, and Control by Neural Network Systems," Ph.D. Dissertation, Department of Engineering Science and Mechanics, Virginia Polytechnic Institute and State Univ., Blacksburg, VA, 2004.

[18] Liu, D. D., Kao, Y. F., and Fung, K. Y., "An Efficient Method for Computing Unsteady Transonic Aerodynamics of Swept Wings with Control Surfaces," *Journal of Aircraft*, Vol. 25, No. 1, 1988, pp. 25–31. doi:10.2514/3.45536

[19] Drela, M., "XFOIL: An Analysis and Design System for Low Reynolds Number Airfoils," *Conference Proceedings on Low Reynolds Number Aerodynamics*, Notre Dame, IN, June 1989.

[20] Abbott, I. H., and Von Doenhoff, A. E., *Theory of Wing Sections-Including a Summary of Airfoil Data*, Dover, New York, 1959.

[21] Rice, M. S., *Handbook of Airfoil Sections for Light Aircraft*, Aviation Publications, Milwaukee, WI, 1971.